crystals

MDPI

Article

Towards High-Performance Heat-Resistant Magnesium Alloys: The Role of Mn in Asymmetric Extruded Mg-Al-Sn-Ca Alloys

Ding-Hao Xu [1], Xu Guo [2], Dian-Mai Zhou [1], Wen-Xue Zhao [1], Dong-Ri Xu [1], Hao-Cheng Leng [1], Yong-Xin Qu [1], Hao Liu [1], Ning Zhang [1], Bai-Tong Zhou [1], Jin-Long Cai [2] and Zhi-Gang Li [2,*]

[1] National Railway Vehicle Engineering Research Center, CRRC Changchun Railway Vehicles Co., Ltd., Changchun 130062, China; xudinghao.ck@crrcgc.cc (D.-H.X.)
[2] Key Laboratory of Automotive Materials Ministry of Education, School of Material Science and Technology, Jilin University, Changchun 130022, China; jlcai23@mails.jlu.edu.cn (J.-L.C.)
* Correspondence: lzg@jlu.edu.cn

Abstract

This work systematically investigates the influence of Mn content (0.1, 0.3, and 0.5 wt.%) on the microstructure, mechanical properties, and high-temperature stability of asymmetric extruded Mg-4.0Al-0.8Sn-0.3Ca-xMn alloys. The results demonstrate that Mn addition effectively promotes the formation of multi-scale secondary phases. Increasing the Mn content refines the average grain size from ~2.82 μm to ~1.89 μm and significantly modulates the recrystallization behavior of the alloy. The ATX4103-05Mn alloy (0.5 wt.% Mn) exhibits an optimal strength–ductility synergy, achieving a yield strength of 281.8 MPa and an elongation of 19.1%. Quantitative analysis reveals that this enhancement is predominantly governed by dispersion strengthening ($\Delta\sigma_p$~34.1 MPa), with supplementary contributions from grain boundary and dislocation strengthening. Furthermore, the ATX4103-05Mn alloy shows superior resistance to abnormal grain growth after thermal exposure at 400 °C for 10 h, which is attributed to effective Zener pinning by the uniform distribution of short rod-shaped Al8Mn5 phases along the grain boundaries. This study elucidates the multi-scale strengthening and thermal stabilization mechanisms enabled by Mn microalloying, providing a viable pathway for developing high-performance, thermally stable magnesium alloys.

Keywords: magnesium alloy; asymmetric extrusion; high-temperature thermal exposure; Mn addition

1. Introduction

Magnesium alloys are recognized as promising lightweight and high-strength structural materials [1,2]. Their low density, high specific strength, excellent damping capacity, and effective electromagnetic shielding properties have drawn significant attention in fields such as aerospace, automotive engineering, and electronics, aligning with the urgent demands for energy conservation and sustainable development [3,4]. Severe plastic deformation (SPD) techniques have been widely recognized for their ability to introduce large plastic strains and enhance the mechanical performance of magnesium alloys. For instance, multi-directional forging has been shown to effectively refine grain structures and improve strength–ductility synergy in Mg rare earth alloys [5]. Among these techniques, asymmetric extrusion offers unique advantages by introducing intense shear strain during processing, which has been demonstrated to effectively refine the grain structure and improve the mechanical strength of magnesium alloy sheets [6]. However, conventional magnesium

Check for updates

Received: 7 February 2026
Revised: 23 February 2026
Accepted: 27 February 2026
Published: 28 February 2026

Copyright: © 2026 by the authors. Licensee MDPI, Basel, Switzerland. This article is an open access article distributed under the terms and conditions of the Creative Commons Attribution (CC BY) license.

alloys often suffer from pronounced abnormal grain growth (AGG) after exposure to temperatures between 400 °C and 500 °C [7,8], which severely restricts their application in critical high-temperature components [9–12]. Therefore, developing novel heat-resistant magnesium alloys that simultaneously offer good room-temperature mechanical performance and high-temperature microstructural stability remains a key research objective in this field.

Among various alloy systems, the Mg-Al-Sn system has been extensively studied due to its ability to form the thermally stable Mg_2Sn phase [13,14]. To further enhance the overall performance, the addition of Ca has been shown to refine grains and improve heat resistance by forming nano-sized CaMgSn precipitates [15,16]. However, excessive Ca often leads to coarse eutectic phases and a consequent deterioration in ductility [6,17]. In recent years, Mn has emerged as an effective microalloying element that plays a unique role in tailoring the microstructure and properties of magnesium alloys [18,19]. Mn exhibits low solid solubility in the Mg matrix and readily forms thermally stable Al-Mn intermetallic compounds (e.g., Al_8Mn_5) with Al [20]. As demonstrated by Qin et al. [21], have demonstrated that trace Mn additions can significantly refine grains, thereby enhancing strength through grain boundary strengthening. Furthermore, finely dispersed Al_8Mn_5 nanoparticles can provide notable precipitation strengthening [22,23].

In terms of improving heat resistance, the contribution of Mn is particularly significant. The high-melting-point Al–Mn phases formed by Mn can effectively inhibit grain boundary migration and grain growth through the Zener pinning mechanism, while also impeding dislocation climb and dynamic recovery processes [24,25]. These characteristics enable Mn-containing magnesium alloys to maintain excellent microstructural stability even under high-temperature conditions.

Although existing studies have preliminarily revealed the positive effects of Mn on the room-temperature mechanical properties and high-temperature stability of magnesium alloys, a systematic understanding of its role in microstructural evolution during asymmetric extrusion, texture modification, and the mechanisms underlying microstructural stability after high-temperature exposure remains limited. This work aims to comprehensively investigate the influence of Mn content on the microstructure, room-temperature mechanical properties, and high-temperature thermal stability of Mg-Al-Sn-Ca-xMn alloy sheets. It seeks to elucidate the multi-scale strengthening–toughening and thermal stabilization mechanisms, thereby providing theoretical foundations and processing guidance for the development of high-performance thermally stable magnesium alloys.

2. Materials and Methods

2.1. Material Preparation

Magnesium alloy ingots with nominal compositions of Mg-4.0Al-0.8Sn-0.3Ca-xMn (x = 0.1, 0.3, and 0.5 wt.%) were prepared via sub-rapid solidification (SRS) using a water-cooled copper mold. The alloys were melted in an electric resistance furnace under a protective atmosphere of 1% CO_2 and 99% SF_6, starting from commercial pure Mg (99.85 wt.%), pure Al (99.90 wt.%), pure Sn (99.90 wt.%), Mg-20 wt.% Ca master alloy, and Mg-5 wt.% Mn master alloy. According to their Mn contents, the alloys are designated as ATX4103-01Mn (x = 0.1), ATX4103-03Mn (x = 0.3), and ATX4103-05Mn (x = 0.5). The ingots were cut into extrusion billets with dimensions of 10 mm × 50 mm × 65 mm by wire electrical discharge machining. These billets were subsequently subjected to the stepwise solid-solution treatment shown in Figure 1 to ensure complete dissolution of alloying elements without incipient melting. Asymmetric extrusion was performed using the die illustrated in Figure 1, which has an asymmetric ratio of 3:2 (length ratio of the two sides at the extrusion outlet) and an extrusion ratio of 21:1. Prior to extrusion, the billets were held at 400 °C

for 1 h and then immediately transferred to a die pre-heated to 100 °C. Extrusion was carried out at a ram speed of 16 mm/s to produce plates with a cross-sectional dimension of 2 mm × 20 mm. To evaluate the high-temperature thermal stability, the extruded plates were subsequently held at 400 °C for 10 h.

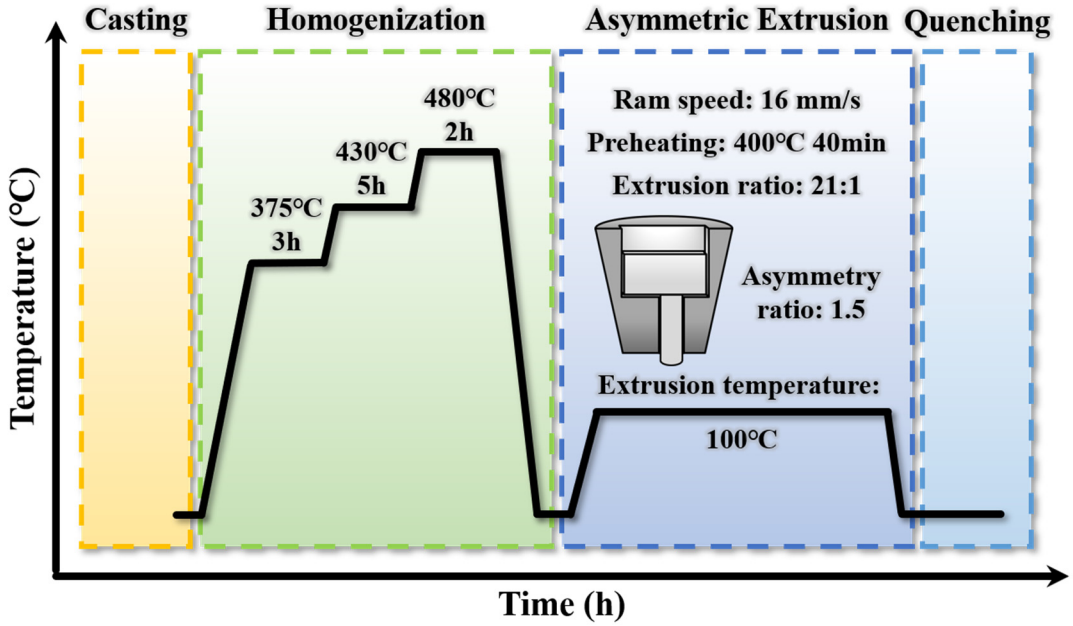

Figure 1. Schematic of the asymmetric extrusion process.

2.2. Mechanical Property Tests

Tensile specimens with a dog-bone geometry were machined along the extrusion direction (ED) of the as-extruded sheets, featuring a gauge length of 10 mm, a width of 4 mm, and a thickness of 2 mm. Tensile tests were conducted on a Shimadzu AGS-100 kN universal testing machine at a constant strain rate of 1×10^{-3} s^{-1}. To ensure the reproducibility of the results, a minimum of three specimens were tested for each alloy.

2.3. Microstructure Characterizations

Microstructural characterization was conducted at multiple scales. Elemental and secondary phase distributions were analyzed using a scanning electron microscope (SEM, Sigma 500, Zeiss, Oberkochen, Germany) equipped with an energy-dispersive X-ray spectrometer (EDS, Oxford Ultim Max, Oxford, UK). Grain orientation characteristics were subsequently examined via electron backscatter diffraction (EBSD, Oxford Symmetry, Oxford, UK) attached to the SEM. Nanoscale information was obtained using a transmission electron microscope (TEM, Talos-F200X, Thermo Fisher, Waltham, MA, USA). The preparation of EBSD samples involved sequential mechanical grinding with progressively finer SiC papers (#600, #2000, #5000, #7000), followed by electropolishing at 20 V, 0.2 A, and −20 °C for 90 s. TEM samples were prepared by mechanically grinding to approximately 30 μm, followed by final thinning with a liquid-nitrogen-cooled ion beam mill (Fischione TEM Mill 1051, Fischione Instruments, Export, PA, USA). Phase identification was conducted by X-ray diffraction (XRD, Rigaku 18KW/D/Max 2500 PC, Rigaku, Tokyo, Japan) using Cu Kα radiation.

3. Results

3.1. Microstructures of ATX4103-xMn Alloys

3.1.1. Microstructure and Phases of ATX4103-xMn Alloys

Figure 2 displays the microstructure of sub-rapidly solidified (SRS) Mg-4.0Al-0.8Sn-0.3Ca-xMn alloys (x = 0.1, 0.3, 0.5 wt.%). In the as-cast sample, three distinct morphologies of secondary phases are predominantly observed: coarse white bone-shaped secondary phases, gray spherical secondary phases, and relatively fine short rod or spherical white secondary phases. Furthermore, as the Mn content increases from 0.1 wt.% to 0.3 wt.%, the area fraction of secondary phases rises from approximately 1.98% to about 3.03%. With the addition of 0.5 wt.% Mn, the fraction further increases to approximately 3.73%. These results indicate that the area fraction of secondary phases in the alloy increases with increasing Mn content.

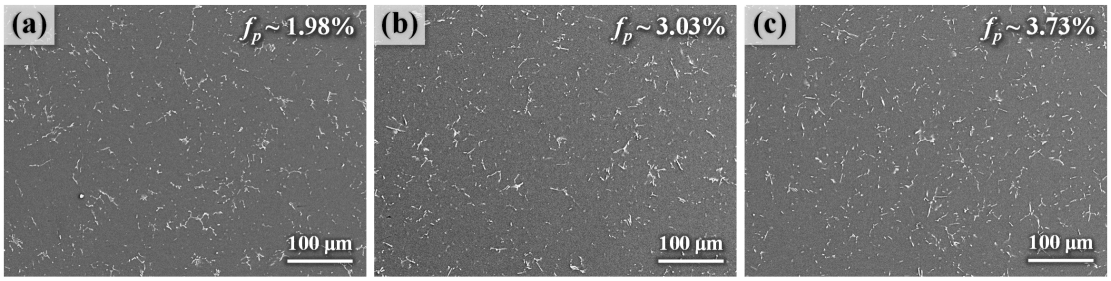

Figure 2. SEM images of the as-cast alloys: (**a**) ATX4103-01Mn, (**b**) ATX4103-03Mn, (**c**) ATX4103-05Mn.

As shown in Figure 3, the phase composition of as-cast ATX4103-xMn alloys was analyzed by XRD. Characteristic peaks corresponding to the CaMgSn, Al_2Ca, and $Mg_{17}Al_{12}$ phases were detected in all three samples. Among these, the CaMgSn phase exhibits relatively high peak intensities, whereas the Al_2Ca and $Mg_{17}Al_{12}$ phases show comparatively lower peak intensities, suggesting that the CaMgSn phase likely possesses a larger volume fraction in all the alloys investigated. In addition, diffraction peaks of the Al_8Mn_5 phase were identified. This can be attributed to the extremely low solid solubility of Mn in magnesium alloys at room temperature, coupled with the presence of 4 wt.% Al in the system, which strongly promotes the formation of the Al_8Mn_5 phase [26].

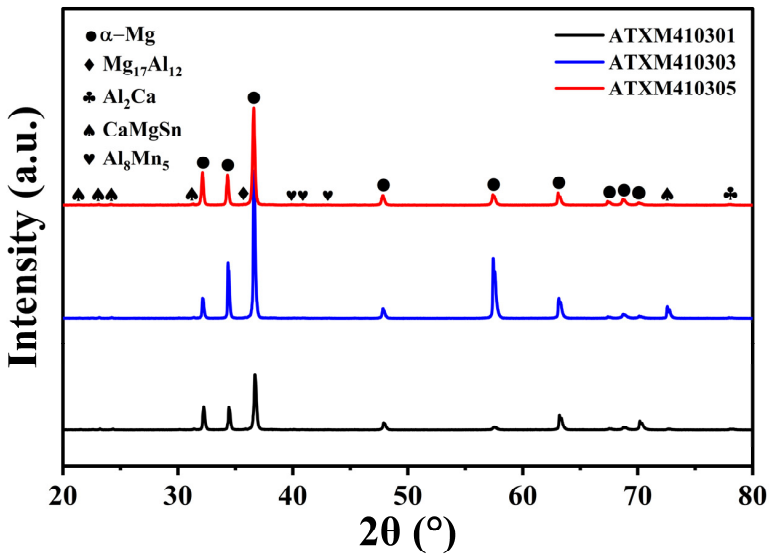

Figure 3. XRD patterns of the as-cast ATX4103-xMn alloys (x = 0.1, 0.3, and 0.5 wt.%). The phases were identified using the following PDF cards: Mg (00-035-0821), $Mg_{17}Al_{12}$ (00-001-1128), Al_2Ca (01-025-0875), Al_8Mn_5 (00-032-0021), and CaMgSn (04-003-2685).

Figure 4 presents the EDS elemental mapping results of the regions shown in Figure 2 for further analysis of the secondary phase composition. In the ATX4103-01Mn alloy (Figure 4a), bone-shaped CaMgSn phases and a minor amount of Al_2Ca phase are predominantly observed. When the Mn content increases to 0.3 wt.% (Figure 4b), distinct short rod and spherical secondary phases appear in addition to the previously mentioned phases; based on their elemental distribution, these are identified as Al_8Mn_5 phases. Furthermore, in the ATX4103-05Mn alloy (Figure 4c), the Al_8Mn_5 phases form a continuous network and exhibit a noticeable increase in volume fraction. These results confirm that raising the Mn content elevates the area fraction of the Al_8Mn_5 phase, which aligns with the statistical findings reported earlier.

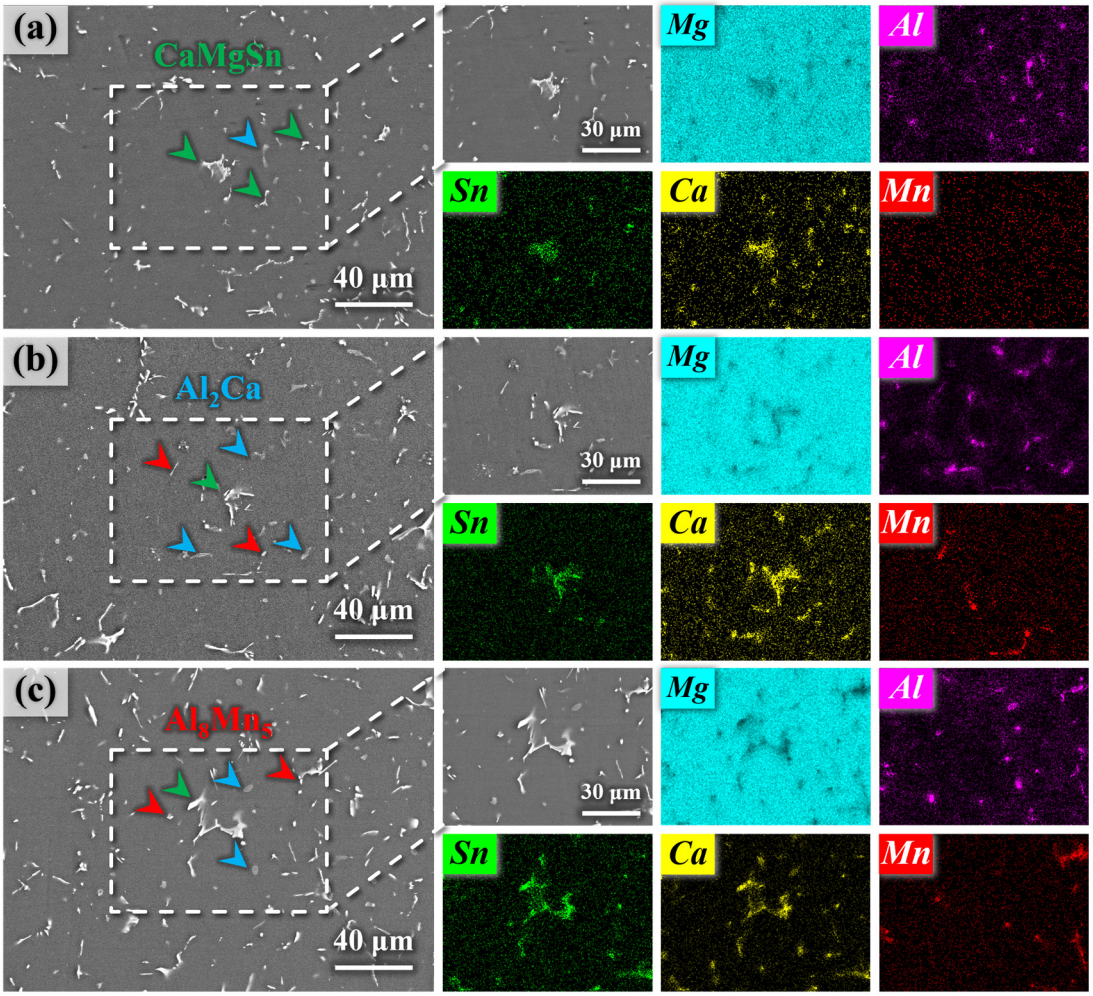

Figure 4. SEM images and corresponding EDS elemental maps of the as-cast alloys: (**a**) ATX4103-01Mn, (**b**) ATX4103-03Mn, (**c**) ATX4103-05Mn.

Figure 5 shows the SEM images and corresponding EDS mapping results of the ATX4103-xMn alloys after stepwise solid solution treatment. As presented in Figure 5b, in the solution-treated ATX4103-03Mn sample, the Al_2Ca phase is almost completely dissolved back, while the CaMgSn phase remains intact. This is likely attributable to its higher melting point (the melting point of the CaMgSn phase is 1184 °C [27,28]). The same phenomenon is observed in the ATX4103-05Mn sample (Figure 5c). Furthermore, in the solution-treated ATX4103-05Mn sample shown in Figure 5c, a small portion of the Al_8Mn_5 phase has dissolved, but the coarse, continuously distributed Al_8Mn_5 phase is largely retained.

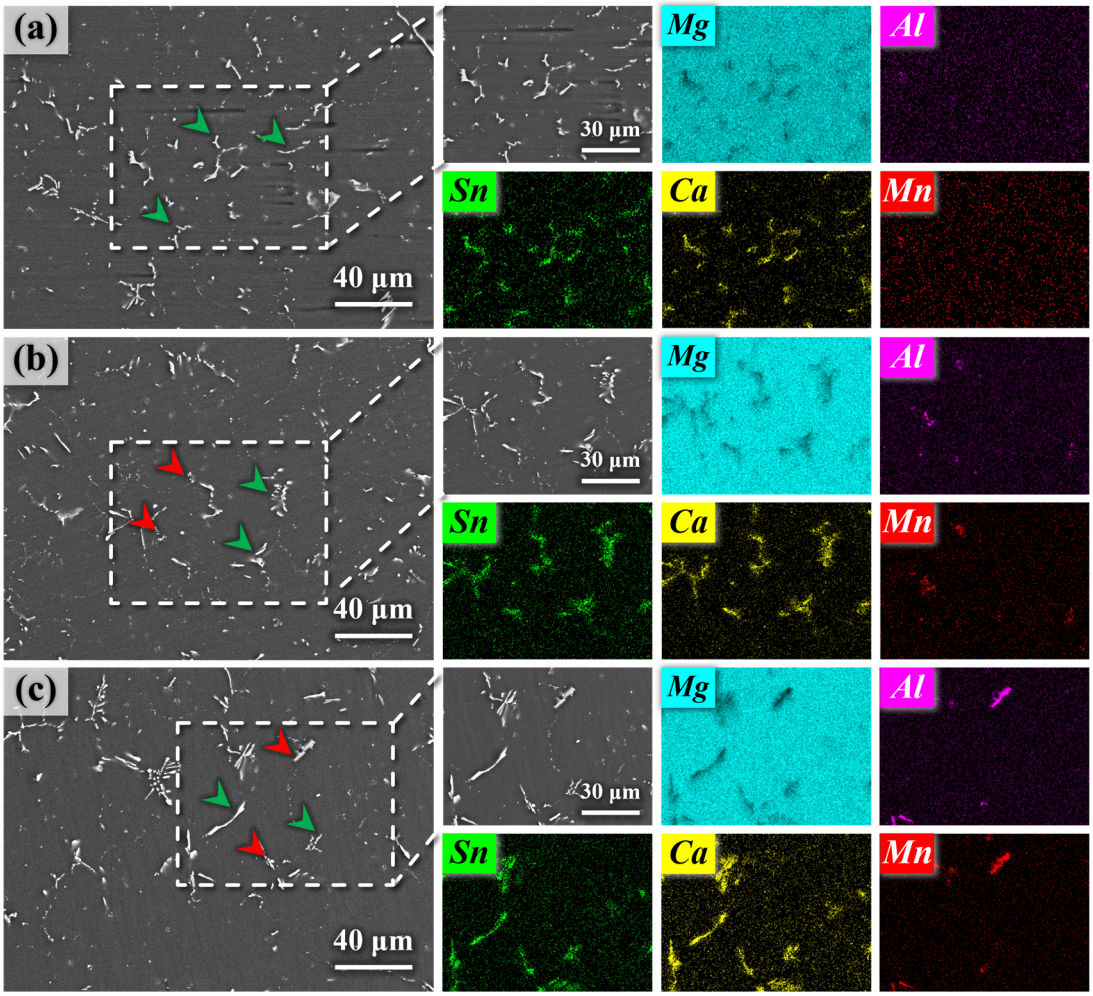

Figure 5. SEM images and corresponding EDS elemental maps of the solution-treated alloys: (**a**) ATX4103-01Mn, (**b**) ATX4103-03Mn, (**c**) ATX4103-05Mn.

Subsequently, the three ATX4103-xMn alloys were subjected to asymmetric extrusion at a die temperature of 100 °C. Figure 6 presents the SEM images and corresponding EDS results of the as-extruded alloys. The coarse secondary-phase particles present in the as-cast microstructure underwent significant fragmentation after solid-solution treatment and asymmetric extrusion, transforming into fine, dispersed particles. These particles exhibit a distinct flow-line distribution along the extrusion direction, forming a characteristic extruded microstructure. Combined with EDS analysis, the secondary phases in the extruded sheets are confirmed to consist mainly of the CaMgSn and Al_8Mn_5 phases. Furthermore, statistical analysis of the area fraction of secondary phases in the extruded alloys reveals a notable increase with higher Mn content. The area fraction rises from 4.6% in ATX4103-01Mn to 5.6% in ATX4103-03Mn. When the Mn content reaches 0.5 wt.%, the area fraction increases significantly to 7.9%, accompanied by the appearance of numerous continuously distributed Al_8Mn_5 phases. This indicates that Mn content plays an important role in influencing the distribution and morphology of secondary phases.

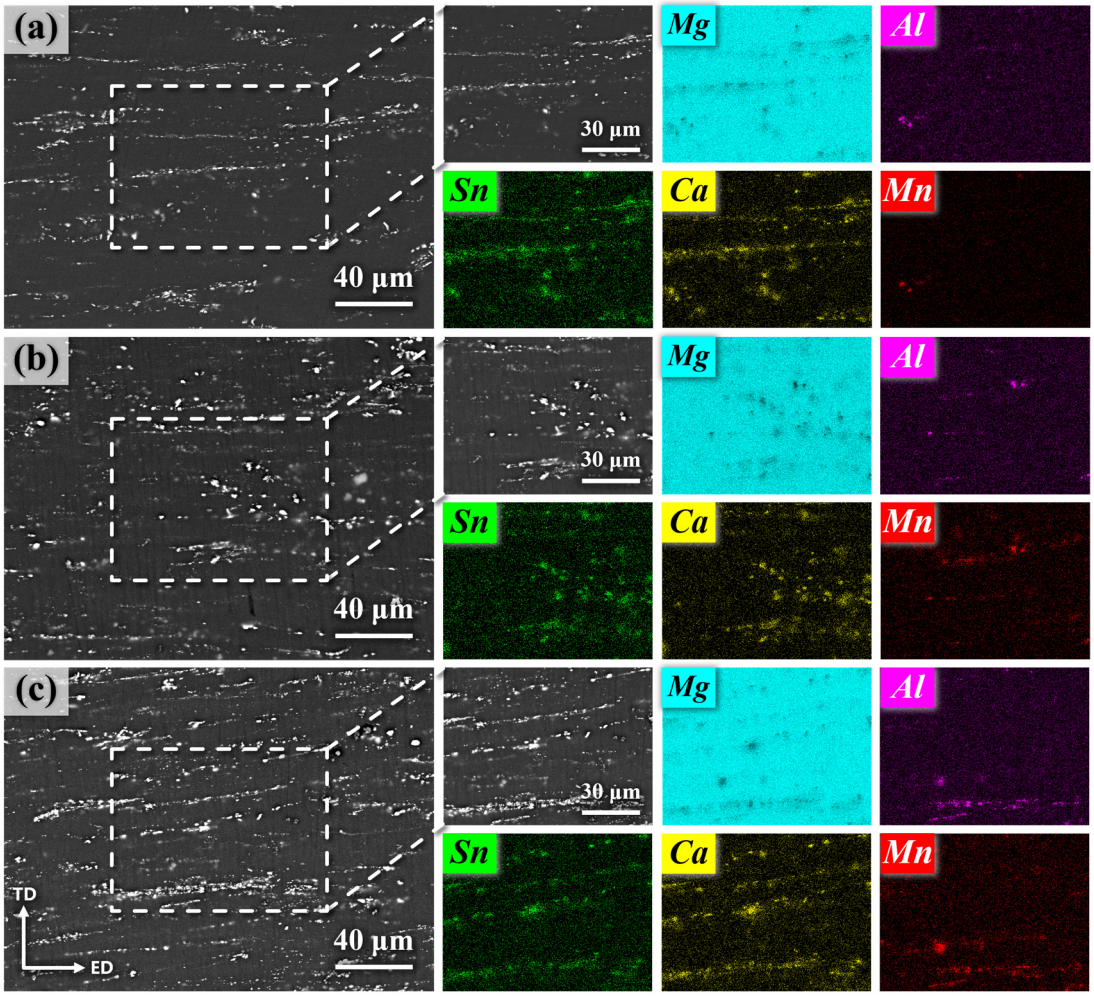

Figure 6. SEM images and corresponding EDS elemental maps of the extruded alloys: (**a**) ATX4103-01Mn, (**b**) ATX4103-03Mn, (**c**) ATX4103-05Mn.

It is worth noting that micron-sized secondary-phase particles have been reported to affect the recrystallization process through the particle-stimulated nucleation (PSN) mechanism [29]. Therefore, the relatively coarse secondary-phase particles in the three alloys may have acted as nucleation sites during dynamic recrystallization in the extrusion process. Additionally, in the as-extruded ATX4103-05Mn alloy shown in Figure 6c, a substantial number of submicron-sized secondary-phase particles were observed, which requires further investigation.

As shown in Figure 7, the distribution of submicron-sized secondary phases in the three as-extruded ATX4103-xMn alloys was analyzed by TEM. The HAADF images in Figure 7 reveal that as the Mn content increases from 0.1 wt.% to 0.5 wt.%, the density of secondary phases increases significantly. The volume fractions of submicron secondary phases in the three alloys are 2.08%, 2.44%, and 2.83%, respectively. EDS elemental mapping indicates the presence of both CaMgSn and Al_8Mn_5 phases in all three alloys. Notably, as shown in Figure 7a,b, the Al_8Mn_5 phases in the ATX4103-01Mn and ATX4103-03Mn alloys primarily exhibit a spherical morphology. When the Mn content is increased to 0.5 wt.%, the Al_8Mn_5 phases in the ATX4103-05Mn alloy adopt a short rod morphology, and their density increases markedly (Figure 7c). This morphological transition can be attributed to enhanced solute supersaturation promoting anisotropic growth along preferred crystallographic directions, combined with extrusion-induced fragmentation and reprecipitation [30].

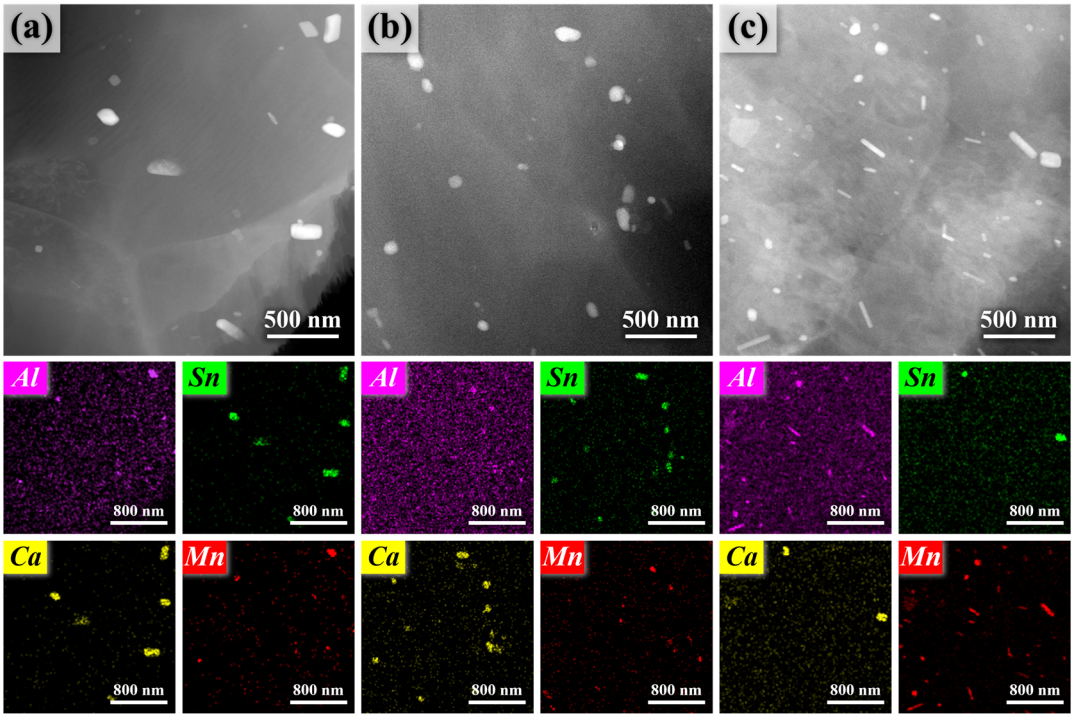

Figure 7. STEM-HAADF images and corresponding EDS elemental maps of the extruded alloys: (**a**) ATX4103-01Mn, (**b**) ATX4103-03Mn, (**c**) ATX4103-05Mn.

The HRTEM images in Figure 8 further provide precise identification of the secondary phase types in the ATX4103-xMn alloys. By comparing the HRTEM images and corresponding fast fourier transform (FFT) patterns with standard PDF cards, the secondary phase shown in Figure 8a is identified as the CaMgSn phase, and that in Figure 8b is confirmed as the Al_8Mn_5 phase.

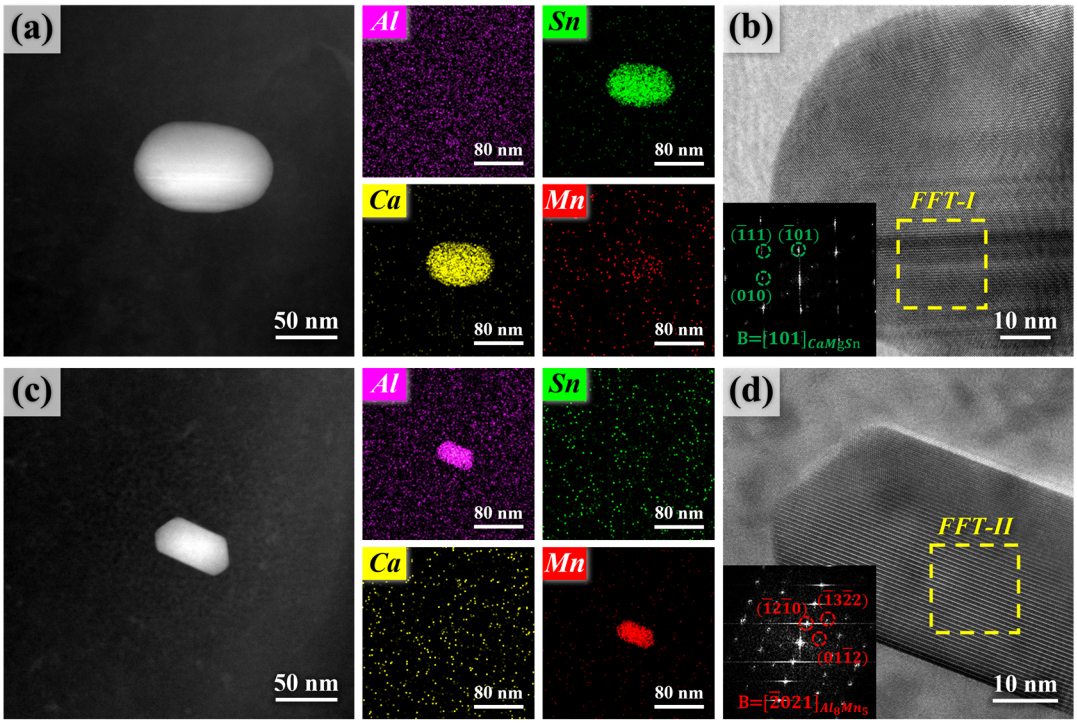

Figure 8. STEM-HAADF images with EDS elemental maps and corresponding HRTEM images with FFT patterns of the (**a**,**c**) CaMgSn and (**b**,**d**) Al_8Mn_5 phases.

3.1.2. Grain Structure of ATX4103-xMn Alloys

Figure 9 presents the EBSD inverse pole figure (IPF) maps and the corresponding grain size statistics for the as-extruded ATX4103-01Mn, ATX4103-03Mn, and ATX4103-05Mn alloys. As shown in Figure 9a, ATX4103-01Mn exhibits a relatively uniform microstructure. In contrast, with increasing Mn content, the as-extruded ATX4103-03Mn and ATX4103-05Mn alloys both exhibit a typical bimodal grain structure [31], consisting of fine dynamic recrystallized (DRXed) grains and coarse un-DRXed regions, as shown in Figure 9b,c. Notably, the extruded ATX4103-03Mn alloy shows significantly larger and non-uniformly distributed un-recrystallized regions. Conversely, the un-recrystallized regions in the extruded ATX4103-05Mn sample appear more dispersed. This divergence is attributed to differences in recrystallization mechanisms activated at different Mn contents, as will be detailed in a subsequent section. Moreover, the average grain sizes of the extruded ATX4103-01Mn, ATX4103-03Mn, and ATX4103-05Mn alloys are approximately 2.82 μm, 2.05 μm, and 1.89 μm, respectively (Figure 9d–f), indicating that increasing the Mn content refines the microstructure.

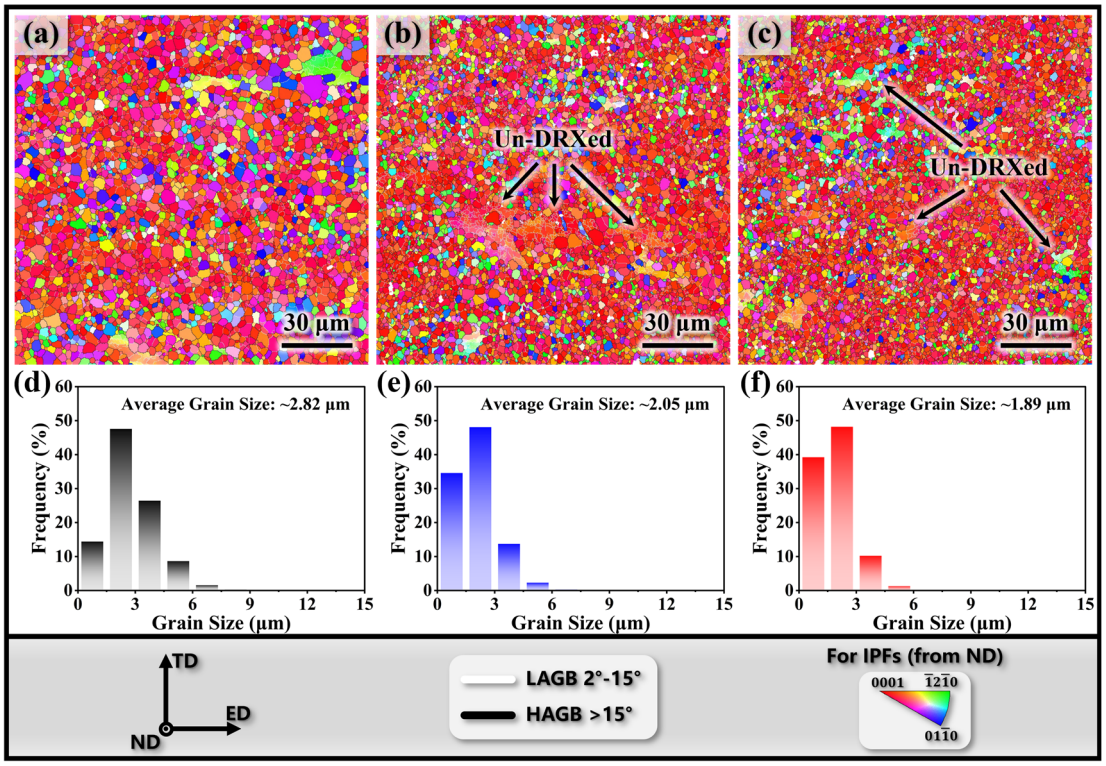

Figure 9. EBSD-IPF maps of the extruded (**a**) ATX4103-01Mn, (**b**) ATX4103-03Mn, (**c**) ATX4103-05Mn alloys, along with the corresponding grain size distribution (**d**–**f**).

Figure 10 shows the kernel average misorientation (KAM) maps of the as-extruded ATX4103-01Mn, ATX4103-03Mn, and ATX4103-05Mn alloys. The ATX4103-01Mn alloy exhibits a low density of dislocations (Figure 10a), corresponding to its low average KAM value of approximately 0.16°. With increasing Mn content, the ATX4103-03Mn and ATX4103-05Mn alloys show higher average KAM values of about 0.29° and 0.30°, respectively. Furthermore, as shown in Figure 10b,c, dislocations are predominantly concentrated within the un-DRXed grains, highlighting a distinct difference in the distribution morphology of the un-DRXed regions between the two alloys.

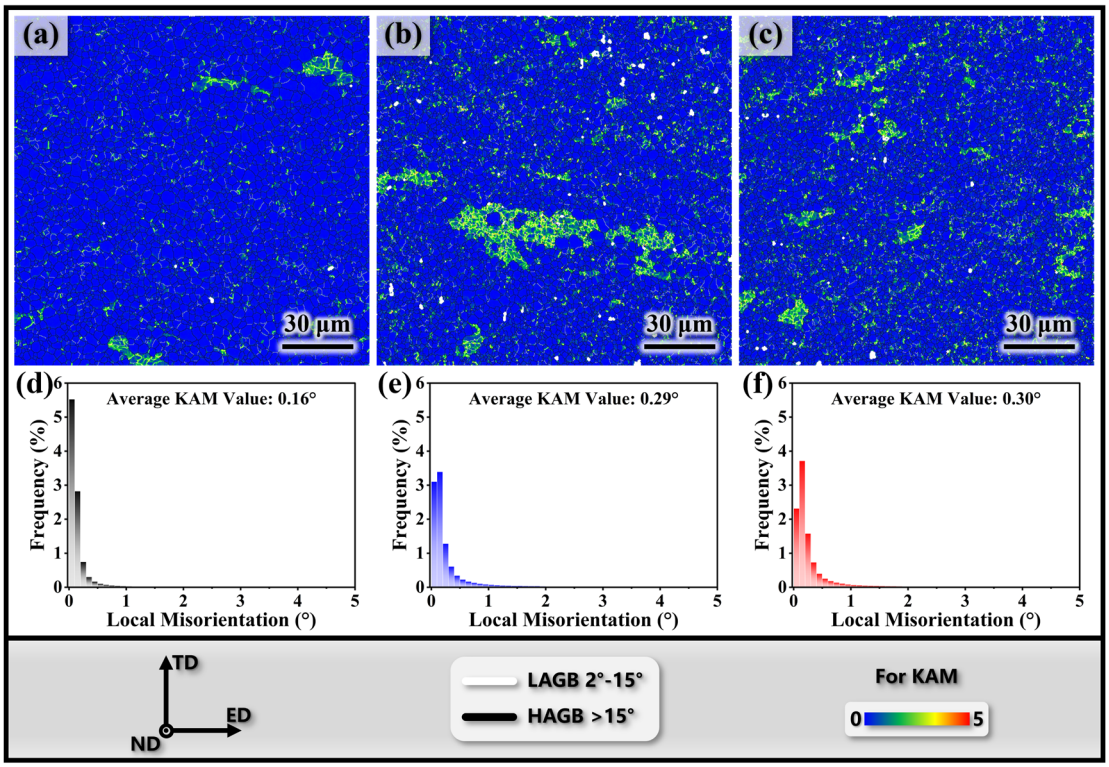

Figure 10. EBSD-KAM maps of the extruded (**a**) ATX4103-01Mn, (**b**) ATX4103-03Mn, (**c**) ATX4103-05Mn alloys, along with the corresponding KAM value distribution (**d**–**f**).

To further elucidate the influence of Mn content on the recrystallization mechanisms, Figure 11 presents the recrystallized grain type maps, basal pole figures, and inverse pole figures of the as-extruded ATX4103-01Mn, ATX4103-03Mn, and ATX4103-05Mn alloys. As shown in Figure 11a, the extruded ATX4103-01Mn alloy is almost fully recrystallized, with a recrystallization fraction of 94.52%. When the Mn content increases to 0.3 wt.%, the recrystallization fraction significantly decreases to 83.30% (Figure 11b), and coarse un-DRXed regions appear. Moreover, the recrystallization fraction of the ATX4103-05Mn alloy is similar to that of ATX4103-03Mn, at 83.32%, but its un-DRXed regions are distributed in a more dispersed manner (Figure 11c).

The formation of texture in magnesium alloys is closely related to the recrystallization process [16]. As shown in Figure 11d–f, the basal textures of the as-extruded ATX4103-01Mn, ATX4103-03Mn, and ATX4103-05Mn alloys exhibit similar morphologies, with poles tilted away from the normal direction (ND) and spread along the transverse direction (TD), which is the typical feature of asymmetric extrusion texture [6]. However, the basal texture intensity shows a non-monotonic variation with increasing Mn content: the texture intensities for ATX4103-01Mn, ATX4103-03Mn, and ATX4103-05Mn alloys are 10.8, 10.3, and 13.4, respectively. This can be attributed to a transition in recrystallization mechanisms dominated by multi-scale (micron-to-nano) secondary phases. In the 0.1Mn alloy, the limited content of nano-scale secondary phases (volume fraction ~2.08%) results in a weakened Zener pinning effect, allowing complete continuous dynamic recrystallization (CDRX) and leading to a relatively large average grain size (~2.82 μm). When the Mn content increases to 0.3 wt.%, the increased volume fraction of nano-scale secondary phases (~2.44%) inhibits the completion of the CDRX process, resulting in the formation of coarse un-DRXed regions. This hindered CDRX progression is further supported by the relatively high texture intensity of ~3.4 and the pronounced $[01\bar{1}0]$//ED fiber texture observed in the inverse pole figure (Figure 11h) [32]. Meanwhile, the increased micro-scale

secondary phases (area fraction ~5.6%) provide additional PSN sites, which contributes to texture weakening [33]. However, a further increase in Mn content to 0.5 wt.% leads to a substantial increase in the volume fraction of nano-scale phases (~2.83%), which significantly enhances the Zener pinning effect [34]. Although the area fraction of micro-scale secondary phases increases markedly to 7.9%, promoting PSN, the migration of grain boundaries is strongly suppressed. This hinders the growth of randomly oriented grains and ultimately results in a microstructure where fine, randomly oriented grains are embedded within a matrix of grains with strong basal orientation, thereby developing a sharper basal texture. Furthermore, the more dispersed distribution of un-DRXed regions in the ATX4103-05Mn alloy contrasts with the coarse un-DRXed regions observed in the ATX4103-03Mn alloy. This difference is attributed to the enhanced PSN effect. The higher area fraction of micron-scale secondary phases (7.9%) in the ATX4103-05Mn alloy provides a greater density of PSN sites, consuming more deformed grains during recrystallization. Consequently, the remaining un-DRXed regions are more uniformly distributed rather than forming large clusters, contributing to the finer and more homogeneous bimodal structure shown in Figure 9c.

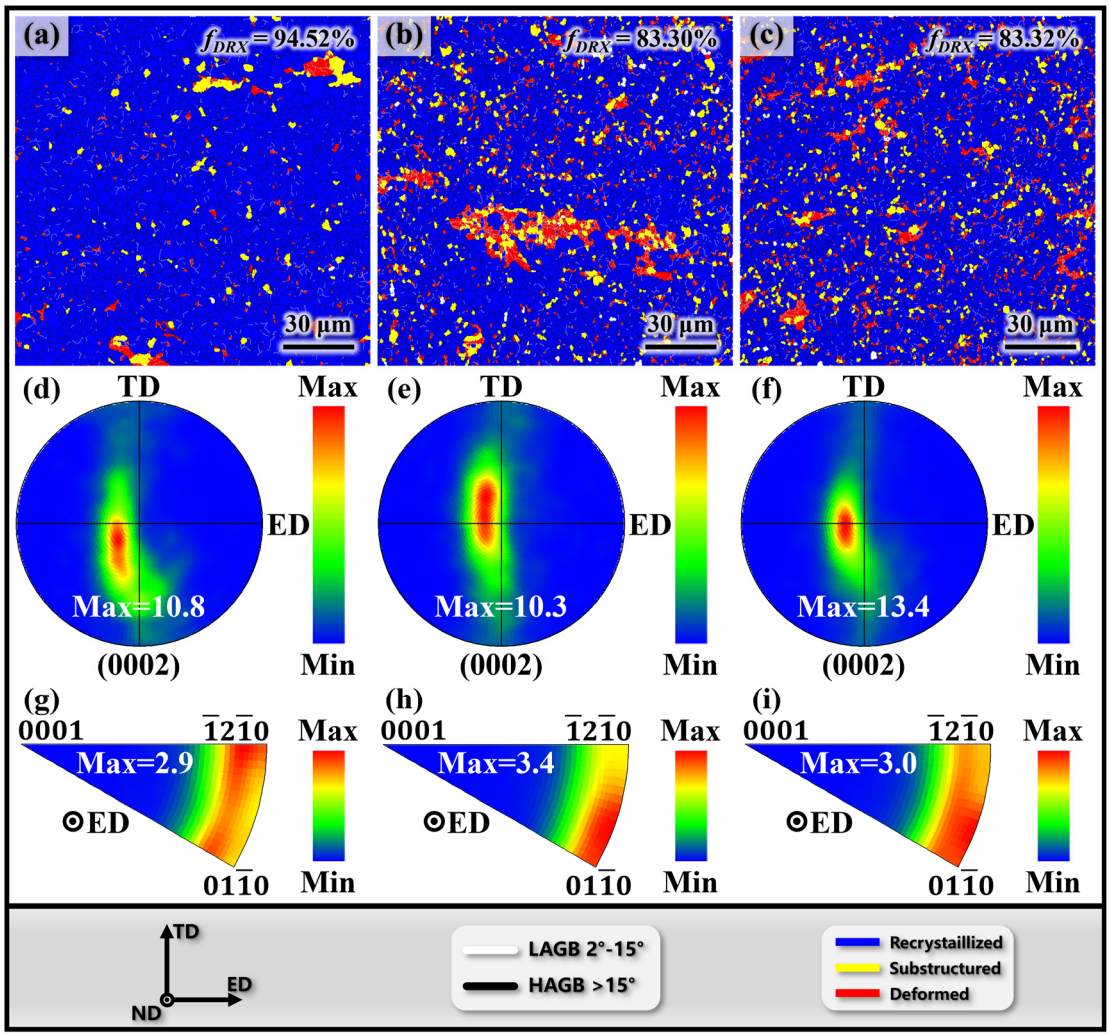

Figure 11. Recrystallized grain type maps of the extruded (**a**) ATX4103-01Mn, (**b**) ATX4103-03Mn, (**c**) ATX4103-05Mn alloys, along with the corresponding (**d**–**f**) pole figures and (**g**–**i**) inverse pole figures.

In summary, secondary phase particles at different scales play a dual role in the recrystallization process: they simultaneously promote recrystallization nucleation and inhibit grain boundary migration. The balance between these two competing effects determines the final microstructure and texture of the alloys.

3.2. Mechanical Properties of ATX4103-xMn Alloys

Figure 12a shows the room-temperature tensile engineering stress–strain curves of the as-extruded ATX4103-xMn (x = 0.1, 0.3, 0.5 wt.%) alloys, with the corresponding mechanical properties listed in Table 1. The results indicate that the addition of trace Mn significantly influences both the strength and ductility of the alloys. As presented in Table 1, the strength properties are markedly enhanced with increasing Mn content. Both the yield strength (YS) and ultimate tensile strength (UTS) exhibit a monotonic increasing trend. From the ATX4103-01Mn to the ATX4103-05Mn alloy, the YS increases from 229.3 MPa to 281.8 MPa, representing an improvement of approximately 22.9%. Similarly, the UTS rises from 313.6 MPa to 357.2 MPa, corresponding to an increase of about 13.9%.

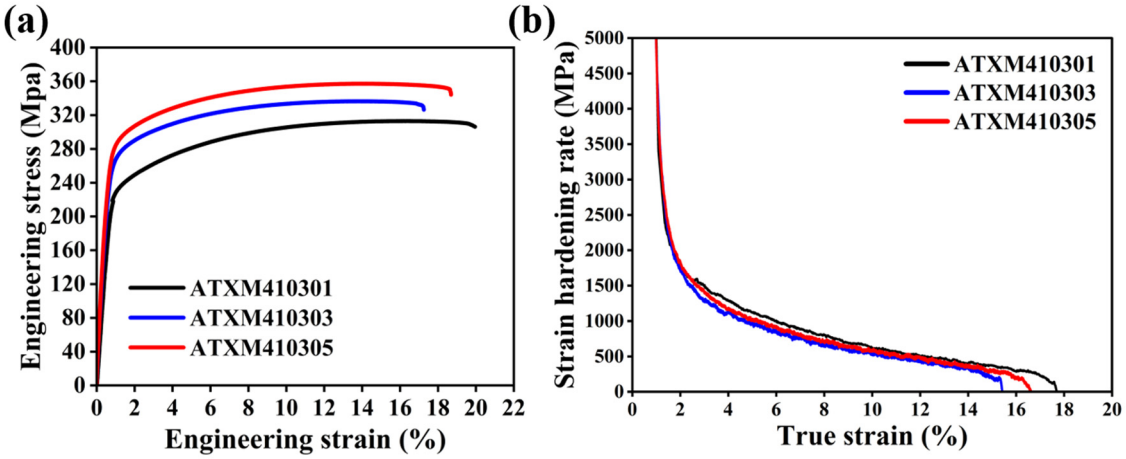

Figure 12. Tensile properties of the extruded alloys: (**a**) engineering stress–strain curves; (**b**) strain hardening rate versus true strain curves.

In contrast, the elongation displays a non-monotonic variation, initially decreasing and then recovering. Specifically, the elongation reaches its lowest value of 17.2% at a Mn content of 0.3 wt.%, which is lower than that of the ATX4103-01Mn alloy (19.8%), and subsequently recovers to 19.1% in the 0.5Mn alloy. Analysis of the work hardening behavior (Figure 12b) reveals that the ATX4103-01Mn alloy exhibits the highest work hardening rate, followed by the ATX4103-05Mn alloy, while the ATX4103-03Mn alloy shows the lowest values. Based on the prior microstructural analysis, the reduced elongation of the ATX4103-03Mn alloy is likely associated with its coarse un-DRXed regions. These regions typically exhibit lower work hardening capacity, leading to stress concentration at the interfaces between fine and coarse grains due to plastic deformation incompatibility [35]. Additionally, the <01-10>//ED fiber texture intensity along the extrusion direction (Figure 11h) reaches its maximum value of 3.4 in ATX4103-03Mn alloy, further exacerbating damage susceptibility [36,37]. In contrast, the ATX4103-05Mn alloy benefits from a more dispersed distribution of un-DRXed regions and a reduced fiber texture intensity (3.0), comparable to that of the ATX4103-01Mn alloy (2.9), both contributing to its recovered ductility of 19.1%.

These findings demonstrate that varying Mn additions influence the recrystallization process through the dynamic precipitation of multi-scale (micro-to-nano) secondary phases, thereby altering the microstructure and ultimately achieving a synergistic enhancement in both strength and ductility.

3.3. Grain Characteristics of ATX4103-xMn Alloys After Thermal Exposure

To investigate the microstructural stability of the asymmetrically extruded ATX4103-xMn (x = 0.1, 0.3, 0.5 wt.%) alloys under high-temperature conditions, the extruded samples were further subjected to static thermal exposure at 400 °C for 10 h. This experiment aimed to systematically evaluate the grain evolution behavior of alloys with different Mn contents during isothermal holding, with particular focus on their grain growth tendencies. The goal is to establish correlations among composition, microstructure, and high-temperature stability, thereby providing a basis for assessing the material's performance in potential high-temperature applications. The microstructures after thermal exposure are presented in Figure 13. As shown in Figure 13a, the ATX4103-01Mn alloy exhibits a typical abnormal grain growth (AGG) microstructure, containing a significant number of notably coarsened grains. Its average grain size increased from 2.82 μm to 11.07 μm. When the Mn content was raised to 0.3 wt.%, the average grain size of the ATX4103-03Mn alloy after exposure grew from 2.05 μm to 8.03 μm, with a noticeable reduction in abnormally grown grains. The ATX4103-05Mn alloy demonstrated the best high-temperature thermal stability. As shown in Figure 13c, its average grain size increased only from 1.89 μm to 6.02 μm after holding at 400 °C for 10 h. Furthermore, as shown in Figure 13d–f, statistics were performed on the abnormally large grains that significantly exceeded the average size in the three alloys after thermal exposure. The results show that with increasing Mn content, the area fraction of abnormally grown grains decreased substantially from 44.9% in ATX4103-01Mn to 13.8% in ATX4103-03Mn, and finally to only 6.7% in ATX4103-05Mn. This further confirms the enhanced high-temperature thermal stability of the ATX4103-05Mn alloy.

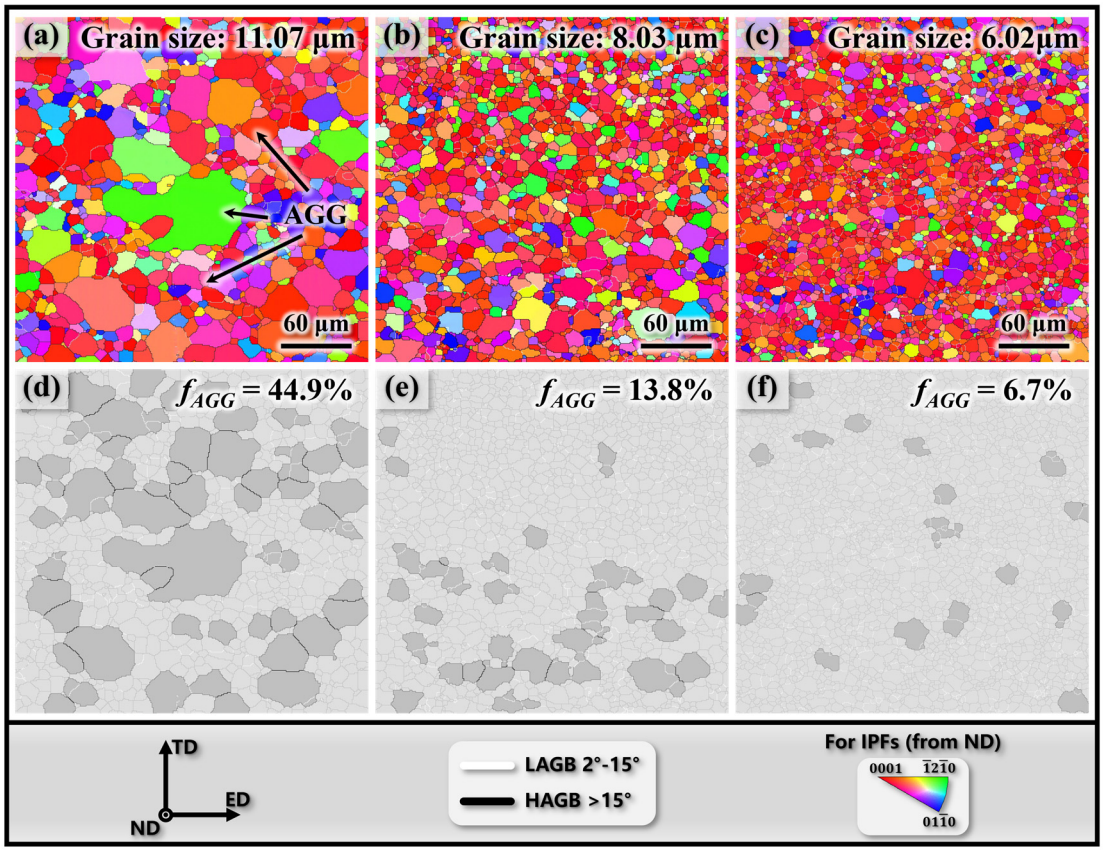

Figure 13. EBSD-IPF maps of the (**a**) ATX4103-01Mn, (**b**) ATX4103-03Mn, (**c**) ATX4103-05Mn alloys after thermal exposure, along with the corresponding AGG distribution maps (**d**–**f**).

Table 1. Room-temperature tensile mechanical properties of extruded ATX4103-xMn alloys (x = 0.1, 0.3, and 0.5 wt.%).

Sample	YS (MPa)	UTS (MPa)	EL (%)
ATX4103-01Mn	$229.3^{+5.7}_{-2.1}$	$313.6^{+2.9}_{-0.6}$	$19.8^{+0.5}_{-1.4}$
ATX4103-03Mn	$262.1^{+0.4}_{-9.9}$	$336.4^{+2.2}_{-9.6}$	$17.2^{+2.0}_{-3.2}$
ATX4103-05Mn	$281.8^{+6.2}_{-1.4}$	$357.2^{+0.9}_{-2.3}$	$19.1^{+0.1}_{-0.6}$

4. Discussion

4.1. Strengthening Mechanisms for ATX4103-xMn Alloys

In this work, the mechanical properties of the asymmetric extruded ATX4103-xMn alloys were significantly improved with increasing Mn content. The addition of Mn promoted the formation of abundant nanoscale Al_8Mn_5 phases during the asymmetric extrusion process, which effectively impeded grain boundary migration and thus resulted in a refined grain structure. During tensile deformation, these nano-scale Al_8Mn_5 phases acted as strengthening particles that hindered dislocation motion, providing dispersion strengthening via the Orowan mechanism. Furthermore, the dislocations retained within the grains contributed to strength enhancement through dislocation interactions. Therefore, the influence of Mn content on the mechanical properties of the asymmetric extruded ATX4103-xMn alloys can be primarily attributed to the following three strengthening mechanisms: grain boundary strengthening, precipitation strengthening, and dislocation strengthening. Analysis of their respective contributions to the YS elucidates the strengthening mechanisms in the asymmetric extruded ATX4103-xMn alloys.

As shown in Figure 9, the grain sizes of the three asymmetric extruded ATX4103-xMn alloys are progressively refined with increasing Mn content. Taking the ATX4103-01Mn alloy as the reference, the contribution of grain refinement to the YS increment can be described by the Hall–Petch relationship [38]:

$$\Delta\sigma_{GB} = k({d_1}^{-1/2} - {d_2}^{-1/2}) \quad (1)$$

where k is the Hall–Petch coefficient (208 MPa·μm$^{-1/2}$) and d represents the average grain size.

The grain sizes of the asymmetric extruded ATX4103-01Mn, ATX4103-03Mn, and ATX4103-05Mn alloys are 2.82 μm, 2.05 μm, and 1.89 μm, respectively. The calculated contributions of grain boundary strengthening to the YS for the ATX4103-03Mn and ATX4103-05Mn alloys are 9.3 MPa and 11.9 MPa higher, respectively, compared to that of the ATX4103-01Mn alloy.

The variations in strengthening arising from the different distributions of nano-sized phases, introduced by Mn addition in the asymmetric extruded ATX4103-xMn alloys, are evaluated using the following Orowan strengthening equation [39]:

$$\sigma_p = M\frac{Gb}{2\pi\sqrt{1-v}(\frac{0.953}{\sqrt{f}}-1)d_p}ln\frac{d_p}{b} \quad (2)$$

In the above equation, M denotes the Taylor factor; G and ν are material constants (shear modulus ≈ 1.66 × 10^4 MPa, Poisson's ratio = 0.3); b is the Burgers vector (3.2 × 10^{-10} m); d_p and f represent the average diameter and volume fraction of the precipitates, respectively. The distribution of nanoscale secondary phases in each alloy, as quantified in Figure 7, yields volume fractions of 2.08%, 2.44%, and 2.83% for the ATX4103-01Mn, ATX4103-03Mn, and ATX4103-05Mn alloys, respectively. The corresponding average diameters of the secondary phases are 74.5 nm, 41.2 nm, and 40.3 nm. The calculated

contributions of dispersion strengthening to the YS for the ATX4103-03Mn and ATX4103-05Mn alloys are 27.1 MPa and 34.1 MPa higher, respectively, compared to that of the ATX4103-01Mn alloy.

As shown in Figure 10, the dislocation distributions in the three asymmetric extruded ATX4103-xMn alloys vary considerably. The difference in the contribution of dislocation strengthening to the YS is determined by estimating the dislocation density in each sample. The dislocation density can be calculated from the average KAM value obtained in Figure 10 using the following equation [40]:

$$\rho_{GND} = \frac{2\theta}{\mu b} \quad (3)$$

where μ is the EBSD scanning step size (0.3 μm), b is the Burgers vector (| b | = 0.32 nm), and θ represents the average KAM value. The estimated dislocation densities for the ATX4103-01Mn, ATX4103-03Mn, and ATX4103-05Mn alloys are 1.85×10^{13} m^{-2}, 3.36×10^{13} m^{-2}, and 3.47×10^{13} m^{-2}, respectively.

The dislocation strengthening contribution is calculated using the following equation [41]:

$$\Delta\sigma_{dislo} = MGb\alpha\rho_{GND}^{1/2} \quad (4)$$

where M denotes the Taylor factor, G is the shear modulus, b represents the Burgers vector, and α is a constant typically taken as 0.2. Accordingly, the dislocation strengthening contributes an increase in yield strength of 4.0 MPa and 4.3 MPa for the ATX4103-03Mn and ATX4103-05Mn alloys, respectively, compared to the ATX4103-01Mn alloy.

The theoretical calculation results summarized above are compiled in Table 2. A comparison with the actual measured increments reveals an excellent consistency between the calculated and experimental values. Further analysis indicates that the enhancement in dispersion strengthening dominates the performance improvement in the three asymmetric extruded alloys, followed by grain boundary strengthening and dislocation strengthening.

Table 2. Theoretical and calculated yield strength of extruded ATX4103-xMn alloys (x = 0.1, 0.3, and 0.5 wt.%).

Sample	σ_{GB} (MPa)	σ_{p} (MPa)	σ_{dislo} (MPa)	$\Delta\sigma_{Calculated}$ (MPa)	$\Delta\sigma_{Actual}$ (MPa)
ATX4103-01Mn	261.6	35.0	11.7	0	0
ATX4103-03Mn	270.8	62.1	15.8	40.4	32.8
ATX4103-05Mn	273.5	69.1	16.0	50.2	52.5

4.2. Mechanism for Enhanced Thermal Stability

TEM and STEM-EDS were employed to analyze the phase distribution and grain boundary characteristics of the ATX4103-01Mn and ATX4103-05Mn alloys after thermal exposure (400 °C for 10 h). As shown in Figure 14a, abnormally grown grains, with sizes nearly three times larger than those observed in the ATX4103-05Mn alloy (Figure 14b), are present in the ATX4103-01Mn alloy. Furthermore, the distribution of secondary phases within these abnormally grown grains is sparse. Closer examination of the ATX4103-05Mn alloy reveals that its grain boundaries are strongly pinned by nano-sized secondary phases. Observations of three specific regions where grain boundaries interact with secondary phases (Figure 14c–e) show pronounced concavity of the grain boundaries at the pinning sites, indicating effective inhibition of grain boundary migration. STEM-EDS analysis confirms that these short rod-shaped secondary phases are primarily Al_8Mn_5, with a minor presence of spherical CaMgSn phases also distributed along the grain boundaries. It has been reported that rod-shaped nano-particles exert a stronger pinning force on grain boundary migration compared to their spherical counterparts [42]. Therefore, the superior

thermal stability of the ATX4103-05Mn alloy can be attributed to the effective Zener pinning force provided by the uniformly distributed, high-density population of short rod Al_8Mn_5 phases. This stabilizes the grain boundaries and effectively reduces their migration rate during thermal exposure.

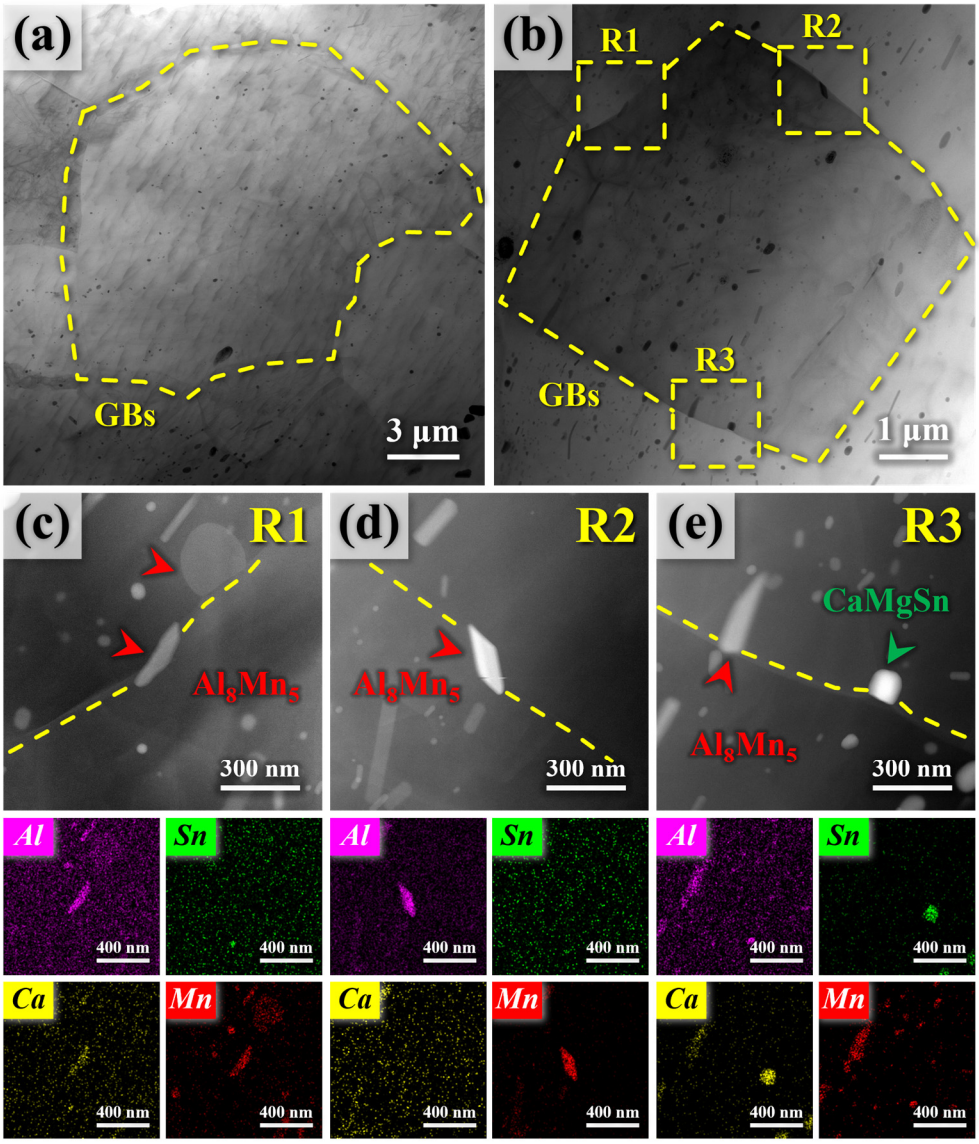

Figure 14. Bright-field TEM images of the (**a**) ATX4103-01Mn and (**b**) ATX4103-05Mn alloys after thermal exposure, along with the (**c**–**e**) STEM-HAADF images and corresponding EDS elemental maps of the regions marked in (**b**).

5. Conclusions

This study demonstrates that the asymmetric extruded Mg-4.0Al-0.8Sn-0.3Ca-xMn (x = 0.1, 0.3, 0.5 wt.%) alloy achieves an excellent balance of strength, ductility, and high-temperature microstructural stability in the ATX4103-05Mn alloy (0.5 wt.% Mn). The key conclusions are as follows:

(1) The recrystallization behaviour and final microstructure are governed by the Mn content. The 0.3Mn alloy develops coarse, non-uniform un-DRXed regions due to inhibited continuous dynamic recrystallization (CDRX). In contrast, enhanced particle-stimulated nucleation (PSN) in the 0.5Mn alloy leads to a finer, more dispersed un-DRXed morphology, refining the average grain size from ~2.82 μm to ~1.89 μm.

(2) The ATX4103-05Mn alloy exhibits an optimal strength–ductility synergy, attaining a yield strength of 281.8 MPa and an ultimate tensile strength of 357.2 MPa. This enhancement stems primarily from dispersion strengthening (∼34.1 MPa), with supplementary contributions from grain boundary strengthening (∼11.9 MPa) and dislocation strengthening (∼4.3 MPa).

(3) Enhanced high-temperature microstructural stability is imparted by the increased Mn content. The ATX4103-05Mn alloy displays the greatest resistance to abnormal grain growth following thermal exposure at 400 °C for 10 h, which is attributed to effective Zener pinning by a uniform, high-density distribution of short rod Al_8Mn_5 phases along the grain boundaries.

Author Contributions: Conceptualization, Z.-G.L.; Methodology, D.-H.X. and J.-L.C.; Validation, D.-H.X., X.G., D.-M.Z., W.-X.Z., D.-R.X., J.-L.C. and Z.-G.L.; Formal analysis, Z.-G.L.; Investigation, X.G., D.-M.Z., W.-X.Z., D.-R.X., H.-C.L., Y.-X.Q., H.L., N.Z., B.-T.Z. and Z.-G.L.; Data curation, D.-H.X., J.-L.C. and Z.-G.L.; Writing—original draft, J.-L.C.; Supervision, X.G., D.-M.Z., H.-C.L., Y.-X.Q., H.L., N.Z., B.-T.Z. and Z.-G.L. All authors have read and agreed to the published version of the manuscript.

Funding: This study was funded by the Jilin Province Science and Technology Development Program (20240301033GX), the National Natural Science Foundation of China (52271031), and the Research and Development Program of China State Railway Group Co., Ltd. (N2024J024).

Data Availability Statement: The original contributions presented in the study are included in the article, further inquiries can be directed to the corresponding author.

Conflicts of Interest: The authors Ding-Hao Xu, Xu Guo, Dian-Mai Zhou, Wen-Xue Zhao, Dong-Ri Xu, Hao-Cheng Leng, Yong-Xin Qu, Hao Liu, Ning Zhang, and Bai-Tong Zhou are employed by the company CRRC Changchun Railway Vehicles Co., Ltd. The authors declare that they have no known competing financial interests or personal relationships that could have appeared to influence the work reported in this paper. The funders had no role in the design of the study; in the collection, analyses, or interpretation of data; in the writing of the manuscript; or in the decision to publish the results.

References

1. Meng, D.; Xu, Y.; Jia, J.; Xu, B.; Hu, L. Achieving strength-ductility synergy of Mg-Gd-Y-Zn-Zr alloy with dense fine-grained microstructure via continuous alternating differential speed extrusion. *J. Mater. Process. Technol.* **2025**, *344*, 119040. [CrossRef]
2. Wang, S.-C.; Chen, S.-Y.; Jin, Z.-Z.; Ma, X.; Jia, H.-L.; Zhu, J.-N.; Li, C.-Y.; Zha, M.; Wang, H.-Y. Dramatic improvement of formability in Mg-3Al-1Sn-0.5Ca-0.1Sm alloy via Mn microalloying combined with high temperature rolling. *J. Magnes. Alloy* **2025**, *13*, 1630–1645. [CrossRef]
3. Li, X.; Fang, X.; Zhang, M.; Zhang, H.; Duan, Y.; Huang, K. Gradient microstructure and prominent performance of wire-arc directed energy deposited magnesium alloy via laser shock peening. *Int. J. Mach. Tools Manuf.* **2023**, *188*, 104029. [CrossRef]
4. Zhang, L.; Yuan, Q.; Tan, J.; Dong, Q.; Lv, H.; Wang, F.; Tang, A.; Eckert, J.; Pan, F. Enhancing the room-temperature plasticity of magnesium alloys: Mechanisms and strategies. *J. Magnes. Alloy* **2024**, *12*, 4741–4767. [CrossRef]
5. Mohammad, F.K.; Rokkala, U.; Mohammed, S.M.A.K.; Altammar, H.; Moinuddin, S.Q.; Mohammed, R. Strength–Ductility Synergy in Biodegradable Mg-Rare Earth Alloy Processed via Multi-Directional Forging. *J. Funct. Biomater.* **2025**, *16*, 391. [CrossRef]
6. Jiang, Y.; Zhang, Z.; Wang, M.; Li, Y.; Cai, J.; Li, Z. Microstructure and mechanical properties of Mg-Al-Sn-Ca alloy extruded by asymmetric severe shear extrusion with different asymmetric coefficients. *J. Alloys Compd.* **2023**, *960*, 170884. [CrossRef]
7. Chen, Q.; Chen, R.; Su, J.; He, Q.; Tan, B.; Xu, C.; Huang, X.; Dai, Q.; Lu, J. The mechanisms of grain growth of Mg alloys: A review. *J. Magnes. Alloy* **2022**, *10*, 2384–2397. [CrossRef]
8. Wang, X.; Guan, D. The evolution of coarse grains and its effects on weakened basal texture during annealing of a cold-rolled magnesium AZ31B alloy. *J. Magnes. Alloy* **2022**, *10*, 1235–1241. [CrossRef]
9. Bian, M.Z.; Sasaki, T.T.; Suh, B.C.; Nakata, T.; Kamado, S.; Hono, K. A heat-treatable Mg–Al–Ca–Mn–Zn sheet alloy with good room temperature formability. *Scr. Mater.* **2017**, *138*, 151–155. [CrossRef]
10. Cihova, M.; Schäublin, R.; Hauser, L.B.; Gerstl, S.S.A.; Simson, C.; Uggowitzer, P.J.; Löffler, J.F. Rational design of a lean magnesium-based alloy with high age-hardening response. *Acta Mater.* **2018**, *158*, 214–229. [CrossRef]

11. Tang, J.; Chen, L.; Zhao, G.; Zhang, C.; Chu, X. Formation mechanism and evolution of surface coarse grains on a ZK60 Mg profile extruded by a porthole die. *J. Mater. Sci. Technol.* **2020**, *47*, 88–102. [CrossRef]
12. Zuiko, I.S.; Mironov, S.; Betsofen, S.; Kaibyshev, R. Suppression of abnormal grain growth in friction-stir welded Al–Cu–Mg alloy by lowering of welding temperature. *Scr. Mater.* **2021**, *196*, 113765. [CrossRef]
13. Mahmudi, R.; Moeendarbari, S. Effects of Sn additions on the microstructure and impression creep behavior of AZ91 magnesium alloy. *Mater. Sci. Eng. A* **2013**, *566*, 30–39. [CrossRef]
14. Wei, F.; Zhou, S.; Wang, J.; Shi, B.; Jin, P.; Ding, Y.; Guo, X. Effect of extrusion temperature on microstructure, mechanical properties and corrosion resistance of Mg-6Sn-3Al-1Zn alloy. *Mater. Today Commun.* **2023**, *37*, 107328. [CrossRef]
15. Li, Y.-X.; Wang, M.-H.; Deng, H.; Jia, H.-L.; Cai, J.-L.; Li, Z.-G. A novel strategy to achieve uniform ultrafine grains in Mg-Al-Sn-Ca alloy via pre-twinning combined with differential-thermal asymmetric extrusion. *Mater. Sci. Eng. A* **2024**, *916*, 147297. [CrossRef]
16. Zha, M.; Wang, S.-C.; Jia, H.-L.; Yang, Y.; Ma, P.-K.; Wang, H.-Y. Effect of minor Ca addition on microstructure and mechanical properties of a low-alloyed Mg–Al–Zn–Sn alloy. *Mater. Sci. Eng. A* **2023**, *862*, 144457. [CrossRef]
17. Li, Y.; Wang, M.; Cai, J.; Wang, C.; Deng, H.; Li, Z. Effect of Ca addition on microstructure and mechanical properties of Mg–3.8Al–1.1Sn alloys. *Mater. Today Commun.* **2024**, *38*, 108204. [CrossRef]
18. Meng, Z.-Y.; Wang, C.; Hua, Z.-M.; Zha, M.; Wang, H.-Y. Achieving extraordinary thermal stability of fine-grained structure in a dilute magnesium alloy. *Mater. Res. Lett.* **2022**, *10*, 797–804. [CrossRef]
19. Robson, J.D.; Henry, D.T.; Davis, B. Particle effects on recrystallization in magnesium–manganese alloys: Particle pinning. *Mater. Sci. Eng. A* **2011**, *528*, 4239–4247. [CrossRef]
20. Li, Z.-G.; Yang, H.-R.; Li, W.-Q.; Guo, X.; Wang, G.-Y.; Song, J.-W. Effect of Mn addition on microstructure and mechanical properties of Mg-2.0Al-0.8Sn-0.5Ca alloys. *J. Alloys Compd.* **2026**, *1050*, 185476. [CrossRef]
21. Qin, G.W.; Ren, Y.; Huang, W.; Li, S.; Pei, W. Grain refining mechanism of Al-containing Mg alloys with the addition of Mn–Al alloys. *J. Alloys Compd.* **2010**, *507*, 410–413. [CrossRef]
22. Li, Z.T.; Qiao, X.G.; Xu, C.; Liu, X.Q.; Kamado, S.; Zheng, M.Y. Enhanced strength by precipitate modification in wrought Mg–Al–Ca alloy with trace Mn addition. *J. Alloys Compd.* **2020**, *836*, 154689. [CrossRef]
23. Nakata, T.; Xu, C.; Ajima, R.; Shimizu, K.; Hanaki, S.; Sasaki, T.T.; Ma, L.; Hono, K.; Kamado, S. Strong and ductile age-hardening Mg-Al-Ca-Mn alloy that can be extruded as fast as aluminum alloys. *Acta Mater.* **2017**, *130*, 261–270. [CrossRef]
24. Shao, L.; Zhang, C.; Li, C.; Tang, A.; Liu, J.; Yu, Z.; Pan, F. Mechanistic study of Mg-Mn-Al extrusion alloy with superior ductility and high strength. *Mater. Charact.* **2022**, *183*, 111651. [CrossRef]
25. Zhang, J.; Peng, P.; Yang, Q.; Luo, A.A. Bimodal grain structure formation and strengthening mechanisms in Mg-Mn-Al-Ca extrusion alloys. *J. Magnes. Alloy* **2023**, *11*, 4407–4419. [CrossRef]
26. Liu, X.Q.; Qiao, X.G.; Pei, R.S.; Chi, Y.Q.; Yuan, L.; Zheng, M.Y. Role of extrusion rate on the microstructure and tensile properties evolution of ultrahigh-strength low-alloy Mg-1.0Al-1.0Ca-0.4Mn (wt.%) alloy. *J. Magnes. Alloy* **2023**, *11*, 553–561. [CrossRef]
27. Lu, X.; Zhao, G.; Zhou, J.; Zhang, C.; Sun, L. Effect of extrusion speeds on the microstructure, texture and mechanical properties of high-speed extrudable Mg–Zn–Sn–Mn–Ca alloy. *Vacuum* **2018**, *157*, 180–191. [CrossRef]
28. Zhang, J.; Liu, B.; Jiang, B.; Yang, H.; Zhou, G.; Dai, J.; Pan, F. Role of secondary phase in microstructural stability of as-extruded Mg–Sn–Ca at high temperature. *Mater. Sci. Technol.* **2016**, *32*, 1818–1825. [CrossRef]
29. Wang, S.; Pan, H.; Xie, D.; Zhang, D.; Li, J.; Xie, H.; Ren, Y.; Qin, G. Grain refinement and strength enhancement in Mg wrought alloys: A review. *J. Magnes. Alloy* **2023**, *11*, 4128–4145. [CrossRef]
30. Wang, D.; Zeng, G.; Xian, J.W.; Nogita, K.; Yasuda, H.; Gourlay, C.M. Growth crystallography and in-situ imaging of nucleation and growth dynamics of Al_8Mn_5 solidifying in AZ magnesium alloys. *Acta Mater.* **2025**, *296*, 121168. [CrossRef]
31. Pan, H.; Qin, G.; Huang, Y.; Ren, Y.; Sha, X.; Han, X.; Liu, Z.Q.; Li, C.; Wu, X.; Chen, H.; et al. Development of low-alloyed and rare-earth-free magnesium alloys having ultra-high strength. *Acta Mater.* **2018**, *149*, 350–363. [CrossRef]
32. Jiang, M.G.; Xu, C.; Yan, H.; Fan, G.H.; Nakata, T.; Lao, C.S.; Chen, R.S.; Kamado, S.; Han, E.H.; Lu, B.H. Unveiling the formation of basal texture variations based on twinning and dynamic recrystallization in AZ31 magnesium alloy during extrusion. *Acta Mater.* **2018**, *157*, 53–71. [CrossRef]
33. Zhang, M.-N.; Jia, H.-L.; Zha, M.; Zhao, L.; Hua, Z.-M.; Wang, C.; Gao, Y.-P.; Wang, H.-Y. Anisotropic segregation-driven texture weakening in a dilute Mg-Al-Ca alloy during isothermal annealing. *Mater. Res. Lett.* **2023**, *11*, 781–788. [CrossRef]
34. Kang, J.-W.; Sun, X.-F.; Deng, K.-K.; Xu, F.-J.; Zhang, X.; Bai, Y. High strength Mg-9Al serial alloy processed by slow extrusion. *Mater. Sci. Eng. A* **2017**, *697*, 211–216. [CrossRef]
35. Dong, X.; Gao, B.; Xiao, L.; Hu, J.; Xu, M.; Li, Z.; Meng, J.; Han, X.; Zhou, H.; Zhu, Y. Heterostructured Metallic Structural Materials: Research Methods, Properties, and Future Perspectives. *Adv. Funct. Mater.* **2024**, *34*, 2410521. [CrossRef]
36. Ning, H.; Wang, C.; Gao, Y.; Zha, M.; Jia, H.-L.; Wang, H.-Y.; Wang, J. Understanding the deformation behaviours of Mg alloys with dispersed non-basal grain-embedded orientation heterostructures. *Acta Mater.* **2024**, *267*, 119727. [CrossRef]

37. Zhao, X.; Li, S.; Zheng, Y.; Liu, Z.; Chen, K.; Yu, J.; Zhang, Z.; Zheng, S. The microstructure evolution, texture weakening mechanism and mechanical properties of AZ80 Mg alloy processed by repetitive upsetting-extrusion with reduced deformation temperature. *J. Alloys Compd.* **2021**, *883*, 160871. [CrossRef]
38. Wang, Q.; Jiang, B.; Tang, A.; He, C.; Zhang, D.; Song, J.; Yang, T.; Huang, G.; Pan, F. Formation of the elliptical texture and its effect on the mechanical properties and stretch formability of dilute Mg-Sn-Y sheet by Zn addition. *Mater. Sci. Eng. A* **2019**, *746*, 259–275. [CrossRef]
39. Zhou, T.; Wang, B.; Li, Y.; Hu, S.; Li, X.; Liu, D. Preparation of ultra-high ductility and high strength Mg-Sn-Zn-Zr alloy by differential thermal ECAP (DT-ECAP) induced heterogeneous structure. *J. Mater. Sci. Technol.* **2024**, *199*, 222–245. [CrossRef]
40. Cai, J.-L.; Liu, P.-L.; Guo, X.; Liu, Q.; Li, Z.-G. High strength-ductility synergy achieved in low-alloyed Mg alloys via hyper-substructure introduction through upsetting-assisted asymmetric extrusion. *J. Magnes. Alloy* **2026**, 101977, *in press*. [CrossRef]
41. Ma, X.; Zha, M.; Wang, S.; Yang, Y.; Jia, H.; Gao, D.; Wang, C.; Wang, H. A rolled Mg−8Al−0.5Zn−0.8Ce alloy with high strength-ductility synergy via engineering high-density low angle boundaries. *J. Magnes. Alloy* **2022**, *10*, 2889–2900. [CrossRef]
42. Chang, K.; Feng, W.; Chen, L.-Q. Effect of second-phase particle morphology on grain growth kinetics. *Acta Mater.* **2009**, *57*, 5229–5236. [CrossRef]

Disclaimer/Publisher's Note: The statements, opinions and data contained in all publications are solely those of the individual author(s) and contributor(s) and not of MDPI and/or the editor(s). MDPI and/or the editor(s) disclaim responsibility for any injury to people or property resulting from any ideas, methods, instructions or products referred to in the content.